

Silicon micropillar electrodes of lithiumion batteries used for characterizing electrolyte additives

Fangrong Hu(胡放荣), Mingyang Zhang(张铭扬), Wenbin Qi(起文斌), Jieyun Zheng(郑杰允), Yue Sun(孙悦), Jianyu Kang(康剑宇), Hailong Yu(俞海龙), Qiyu Wang(王其钰), Shijuan Chen(陈世娟), Xinhua Sun(孙新华), Baogang Quan(全保刚), Junjie Li(李俊杰), Changzhi Gu(顾长志), and Hong Li(李泓)

Citation: Chin. Phys. B, 2021, 30 (**6**): 068202. DOI: 10.1088/1674-1056/abf558
Journal homepage: http://cpb.iphy.ac.cn; http://iopscience.iop.org/cpb

What follows is a list of articles you may be interested in

Suppressing transition metal dissolution and deposition in lithium-ion batteries using oxide solid electrolyte coated polymer separator

Zhao Yan(闫昭), Hongyi Pan(潘弘毅), Junyang Wang(汪君洋), Rusong Chen(陈汝颂), Fei Luo(罗飞), Xiqian Yu(禹习谦), Hong Li(李泓)

Chin. Phys. B, 2020, 29 (**8**): 088201. DOI: 10.1088/1674-1056/ab9610

Design and management of lithium-ion batteries: A perspective from modeling, simulation, and optimization

Qian-Kun Wang(王乾坤), Jia-Ni Shen(沈佳妮), Yi-Jun He(贺益君), Zi-Feng Ma(马紫峰)

Chin. Phys. B, 2020, 29 (**6**): 068201. DOI: 10.1088/1674-1056/ab90f8

Improved electrochemical performance of $Li(Ni_{0.6}Co_{0.2}Mn_{0.2})O_2$ at high charging cut-off voltage with $Li_{1.4}Al_{0.4}Ti_{1.6}(PO_4)_3$ surface coating

Yi Wang(王怡), Bo-Nan Liu(刘柏男), Ge Zhou(周格), Kai-Hui Nie(聂凯会), Jie-Nan Zhang(张杰男), Xi-Qian Yu(禹习谦), Hong Li(李泓)

Chin. Phys. B, 2019, 28 (**6**): 068202. DOI: 10.1088/1674-1056/28/6/068202

Improved electrochemical performances of high voltage $LiCoO_2$ with tungsten doping

Jie-Nan Zhang(张杰男), Qing-Hao Li(李庆浩), Quan Li(李泉), Xi-Qian Yu(禹习谦), Hong Li(李泓)

Chin. Phys. B, 2018, 27 (**8**): 088202. DOI: 10.1088/1674-1056/27/8/088202

Redox-assisted Li^+-storage in lithium-ion batteries

Qizhao Huang(黄启昭) and Qing Wang(王庆)

Chin. Phys. B, 2016, 25 (**1**): 018213. DOI: 10.1088/1674-1056/25/1/018213

Silicon micropillar electrodes of lithiumion batteries used for characterizing electrolyte additives*

Fangrong Hu(胡放荣)[1], Mingyang Zhang(张铭扬)[1,2], Wenbin Qi(起文斌)[2,3], Jieyun Zheng(郑杰允)[2], Yue Sun(孙悦)[2], Jianyu Kang(康剑宇)[2], Hailong Yu(俞海龙)[2], Qiyu Wang(王其钰)[2], Shijuan Chen(陈世娟)[5], Xinhua Sun(孙新华)[5,6], Baogang Quan(全保刚)[2,3,4,†], Junjie Li(李俊杰)[2,‡], Changzhi Gu(顾长志)[2], and Hong Li(李泓)[2,§]

[1] *Guangxi Key Laboratory of Automatic Detecting Technology and Instrument, Guilin University of Electronic Technology, Guilin* 541004, *China*
[2] *Beijing National Laboratory for Condensed Matter Physics, Institute of Physics, Chinese Academy of Sciences, Beijing* 100190, *China*
[3] *University of Chinese Academy of Sciences, Beijing* 10049, *China*
[4] *Songshan Lake Materials Laboratory, Dongguan, China*
[5] *Tianjin Jinniu Power Sources Material Co.,Ltd, Tianjin* 300400, *China*
[6] *Cenertech Tianjin Chemical Research and Design Institute Co.,Ltd, Tianjin* 300131, *China*

(Received 28 February 2021; revised manuscript received 2 April 2021; accepted manuscript online 7 April 2021)

The ⟨100⟩ crystal-oriented silicon micropillar array platforms were prepared by microfabrication processes for the purpose of electrolyte additive identification. The silicon micropillar array platform was used for the study of fluorinated vinyl carbonate (FEC), vinyl ethylene carbonate (VEC), ethylene sulfite (ES), and vinyl carbonate (VC) electrolyte additives in the $LiPF_6$ dissolved in a mixture of ethylene carbonate and diethyl carbonate electrolyte system using charge/discharge cycles, electrochemical impedance spectroscopy, cyclic voltammetry, scanning electron microscopy, and x-ray photoelectron spectroscopy. The results show that the silicon pillar morphology displays cross-shaped expansion after lithiation/delithiation, the inorganic lithium salt keeps the silicon pillar morphology intact, and the organic lithium salt content promotes a rougher silicon pillar surface. The presence of poly-(VC) components on the surface of FEC and VC electrodes allows the silicon pillar to accommodate greater volume expansion while remaining intact. This work provides a standard, fast, and effective test method for the performance analysis of electrolyte additives and provides guidance for the development of new electrolyte additives.

Keywords: lithium-ion batteries, solid electrolyte interphases, electrolyte additives, silicon micropillar electrodes

PACS: 82.45.Yz, 82.45.Fk, 82.47.Aa **DOI:** 10.1088/1674-1056/abf558

1. Introduction

With the increase in the proportion of new energy sources in energy consumption, the users of these new sources have created new challenges for the energy storage capacity of lithium-ion batteries (LIBs).[1,2] In recent years, materials with high specific theoretical capacity have attracted more attention from researchers.[3,4] Silicon (Si) is a promising anode material for LIBs with a high-energy density due to its high specific theoretical capacity of 4200 mAh/g at room temperature, which is ten times higher than that of a widely used graphite anode (372 mAh/g).[5] However, Si anodes suffer from large volume changes ($\sim$ 300%) during cycling. The large volume change of the Si anode causes the Si particles to crack and subsequently isolate the particles, which in turn leads to the continuous decomposition of electrolytes on the newly exposed surface of Si particles during cycling and finally leads to a decrease in the LIB performance.[6] The situation has been greatly improved by employing nanostructured silicon,[7–9] silicon composite electrodes,[10–12] carbon-coated silicon,[13–15] thin-film silicon,[16–18] and new binders.[19–21] However, the preparation process of structured Si anodes is complex and costly, and there are still huge obstacles to commercial applications.

An economical method is to synthesize a robust solid-electrolyte interphase (SEI) film on the surface of Si anodes because the film can prevent volume expansion during the cycling of LIBs. The development of new electrolytes or the incorporation of electrolyte additives is one of the most effective methods to generate a stable SEI and improve the cycle life of Si anodes. As reported previously, the performance of Si anodes can be improved by the incorporation of electrolyte additives such as vinylene carbonate (VC),[22–24] fluoroethylene carbonate (FEC),[25–27] ethylene sulfite (ES),[28,29] vinyl ethylene carbonate (VEC),[30] or alkoxysilanes.[31] These additives provide a certain flexibility that reduces the cracking and re-exposure of the active material, thereby prolonging the

*Project supported by the National Key R&D Program of China (Grant Nos. 2016YFB0100500 and 2016YFB0100100) and the National Natural Science Foundation of China (Grant Nos. 11674387, 11574385, 22005332, 115674368, and 62065005).

†Corresponding author. E-mail: quanbaogang@aphy.iphy.ac.cn
‡Corresponding author. E-mail: lijunjie@iphy.ac.cn
§Corresponding author. E-mail: lihong@iphy.ac.cn

© 2021 Chinese Physical Society and IOP Publishing Ltd

cycle life. However, the understanding of existing electrolyte additives is still insufficient to improve the life of LIBs. Most of the performance tests of the commonly used electrolyte additives mentioned above are carried out using nanosheets, nanofilms, nanoparticles, nanowires, and other structures. The degree of cracking of these test anodes is localized and difficult to observe, and the expansion characteristics of silicon materials are not well displayed. Moreover, the nanosized material has a long cycle life, and the material needs more cycles for cracking and powdering. Therefore, the quick and effective characterization of the influence of electrolyte additives on Si anode materials is an important factor for reducing the research and development cost of electrolyte additives.

To rapidly test electrolyte additives for LIBs, a silicon electrode is required to meet the following criteria: convenient for observation of morphology evolution, short electrochemical test periodicity, and able to analyze the exact components of SEI on a Si electrode. To fulfill the demands mentioned, we prepared Si electrodes with micropillar arrays by microfabrication of a ⟨100⟩-oriented single-crystalline Si substrate. A micropillar array with a regular distribution and proper periodicity and size facilitates the observation of the morphology evolution. The microsized Si pillar can thus influence the cycle performance of the Si electrode material because Si pillars with diameters of several microns are much easier to crack during cycling through the short period test. More importantly, the pure Si pillar electrode with no need to use binders and conductive carbon, such as polyvinylidene fluoride, acetylene black, and graphene, simplifies the chemical environment near the interface between the Si electrode and electrolyte. In this paper, commonly used electrolyte additives (such as FEC, VEC, ES, and VC) were studied in detail for the protection of silicon micropillar arrays. Scanning electron microscopy (SEM) was used to observe the morphological changes of the silicon micropillar array after 10 charge and discharge cycles, and x-ray photoelectron spectroscopy (XPS) was used to detect the SEI film composition to analyze the protection performance of the additive electrochemical cycle products on the Si electrode. The Si micropillar array electrode can not only fulfill the purpose for the evaluation of commercially available electrolyte additives but also accelerate the development of the most proper electrolyte additives for Si-based LIBs.

2. Experimental details

2.1. Materials preparation

Si electrodes used in the LIBs were fabricated by microfabrication processes, as shown in Fig. 1(a). A 4 inch silicon wafer (p-type, 500 ± 10 μm thick, 5–15 Ω/cm, ⟨100⟩ crystal orientation) was first spin-coated with a positive photoresist layer (AZ6130, Merck KGaA, Germany) of ca. 3 μm thick and soft-baked at 100 °C for 3 min for solvent removal prior to photolithography. Then, the wafer was exposed in a contact aligner (Karl Süss MA6, SÜSS MicroTec AG, Germany) with a dose of 100 mJ/cm^2 at 365 nm. The exposed wafer was in turn developed in AZ 300 MIF developer (Merck KGaA, Germany) for 1 min. The pattern in the photoresist layer was transferred to the silicon wafer by a metal deposition and lift-off process. A 50-nm-thick chromium layer was deposited on the wafer by an electron-beam evaporator system (FU-12PEB, F. S. E Corporation, China) and soaked in acetone to form a circular Cr mask (3 μm in diameter) array to be used as an etching mask in the following step. Then, the silicon wafer with the Cr mask was dry-etched into a silicon pillar array using the cryo-etching process with an inductively coupled plasma reactive ion etching system (Oxford PlasmaPro 100 Cobra, Oxford Instruments, UK). SF_6 (45 sccm) and O_2 (11 sccm) were used as the etching gas (12 mTorr) at 4 W of RIE power and 700 W of ICP power, and an etching time of 3 min was used to obtain Si pillars of 10 μm in height. The Cr layer on top of the Si pillars was removed by wet etching in $(NH_4)_2Ce(NO_3)_6/CH_3COOH$ solution for one hour. Finally, the silicon wafer was diced into 5 mm×5 mm tiles using a dicing saw (DAD 323, Disco, Japan).

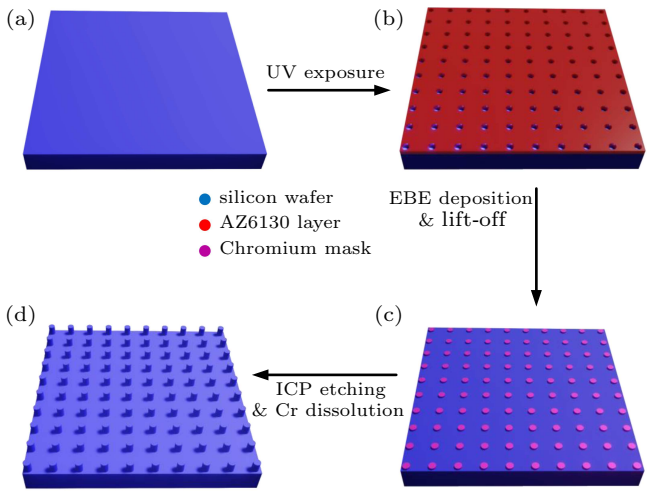


Fig. 1. Schematic of the fabrication of an Si micropillar array. (a) ⟨100⟩ crystalline Si wafer, (b) AZ6130 photoresist for circular hole mask preparation, (c) preparation of Cr metal mask, (d) the ⟨100⟩ crystal Si wafer was etched by ICP and cut to 5 mm×5 mm.

2.2. Electrochemical tests

A coin half-cell (type 2032) was assembled with the Si micropillar array electrode as a working electrode, a separator (polyethylene, PE), and a lithium foil as a counter electrode in an Ar-filled glovebox ($O_2 < 0.1$ ppm, $H_2O < 0.1$ ppm). An electrolyte solution of 1 M $LiPF_6$ dissolved in a mixture of ethylene carbonate (EC) and Dimethyl carbonate (DMC) (1:1 by volume) produced by Tianjin Jinniu Power Supply Material Co., Ltd. was used. ES, VEC, VC, or FEC additives were added at 5 wt% to the electrolyte solution in subsequent exper-

iments. The electrolyte containing additives used are abbreviated in Table 1.

Charge and discharge characteristics were measured at 30 °C using a battery test system (Land BA2100A, Wuhan LAND Electronics Co., Ltd., China). The assembled batteries were galvanostatically tested for 10 cycles, charged to 200 μAh·cm^{-2} and 2.0 V vs. Li^{+}/Li. Cyclic voltammetry (CV) and electrochemical impedance spectroscopy (EIS) were carried out on the batteries through a multichannel potentiostat system (VSP-300, Biologic Science Instruments, France). Each EIS spectrum was recorded between 100 kHz and 100 MHz. The EIS excitation signal had an amplitude of 10 mV. The scanning range of CV was 0–2 V, and the scanning rates were 0.05 mV/s, 0.1 mV/s, 0.15 mV/s, and 0.2 mV/s.

Table 1. The experimental electrolyte composition.

Coin half-cell ID	Electrolyte composition
C-No-Add	1 M $LiPF_6$in EC/DMC(1:1)
C-FEC	1 M $LiPF_6$ in EC/DMC(1:1)+5wt% FEC
C-VEC	1 M $LiPF_6$ in EC/DMC(1:1)+5wt% VEC
C-ES	1 M $LiPF_6$ in EC/DMC(1:1)+5wt% ES
C-VC	1 M $LiPF_6$ in EC/DMC(1:1)+5wt% VC

2.3. Physical characterization

After electrochemical testing, the batteries were disassembled in an argon-filled glove box, where the silicon micropillar electrodes were washed with pure DMC to clean out the residual electrolyte and vacuum dried for hours afterward. Then, the samples were transferred to a scanning electron microscope (Helios 600i, FEI Company, USA) for morphological and structural characterization. The samples were sealed in an argon-filled box for transfer from the glove box to the sample chamber. XPS was performed using a Thermo Fisher spectrometer using monochromatic Al $K\alpha$ radiation at 1486.58 eV. C 1s at 284.8 eV was used as the charge reference to determine the core level binding energy. A pass energy of 160 eV was used for the survey spectra, and 20 eV was used for the narrow regions. The construction and peak fitting of synthetic peaks in narrow region spectra used a Shirley type background, and the synthetic peaks were of a mixed Gaussian–Lorentzian type.

3. Results and discussion

Figure 2 shows the surface morphology of the silicon micropillar array to be used as the working electrode of coin half-cells. From the SEM images obtained with a 45° inclination angle cross sectional view and top view (Figs. 2(a) and 2(b)), the diameter and height of each silicon micropillar are identical, and the silicon micropillars are arranged regularly. The silicon micropillar has a diameter of 3 μm and a height of 6 μm, as shown in Fig. 2(c). The use of micropillars as the working electrode of coin half-cells has several advantages for the investigation of electrolyte additive performance. First, the period of the micropillar array is 10 μm, which is sufficient for accommodating the volume expansion caused by silicon lithiation. Second, the use of Si micropillar arrays as working electrodes avoids the use of binders, conductive additives, and current collectors, which simplifies the chemical environment on the side of the working electrode. Third, the regular arrangement of the Si micropillar array can benefit the SEM observation of the SEI evolution on working electrodes in different states of half-cells with different electrolytes.

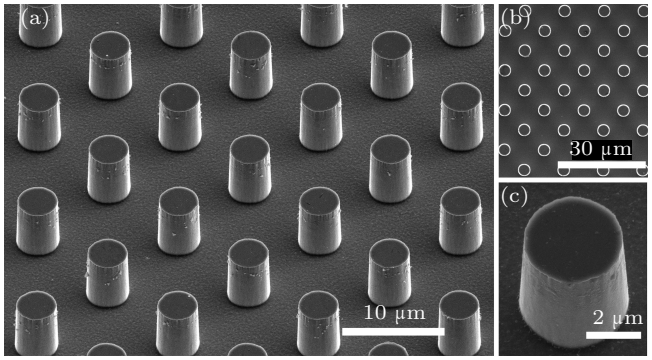


Fig. 2. (a) Cross-sectional SEM image of the as-fabricated silicon micropillar array; (b) and top view of the SEM image; (c) SEM image of a single silicon micropillar.

The capacity behavior of silicon micropillar electrodes was studied in five electrolyte solutions (No-Add, FEC, VEC, ES, and VC) using charge/discharge cycles. Figure 3 shows the data obtained by cycling the half-cells at a current density of 50 μA/cm^2 for 10 cycles at room temperature. The first-cycle charge capacities of C-No-Add, C-FEC, C-VEC, C-ES, and C-VC are 165.1 μAh/cm^2, 149.6 μAh/cm^2, 130 μAh/cm^2, 136.7 μAh/cm^2, and 145.4 μAh/cm^2, respectively (Figs. 3(a)–3(e)). Importantly, the first-cycle discharging capacities of C-FEC, C-VEC, C-ES, and C-VC are lower than that of C-No-Add. We speculate that the reason for the reduced capacities of half-cells with additives is the extra consumption of lithium ions in the electrolyte caused by the SEI-forming additives in the first cycle.[32] The first 3-cycle Coulombic efficiencies of C-FEC, C-VEC, C-ES, and C-VC are obviously lower than that of C-No-Add (Fig. 3(f)), which contradicts the reported observation that electrolyte additives are helpful to improve the Coulombic efficiency of the cells.[33] The insets of Figs. 3(a)–3(e) show that the decrease in the initial charge voltage of the cell gradually stabilizes during cycling. The initial charge voltage of C-No-Add is lower than that of the cell containing the additive, which contradicts the higher Coulombic efficiency of C-No-Add compared to that of the cell containing the additive (as shown in Fig. S2). The decrease in the initial charge voltage implies an increase in the internal polarization resistance of the cell, mainly due to the formation of the SEI film, which increases the resistance at the electrode/electrolyte interface.

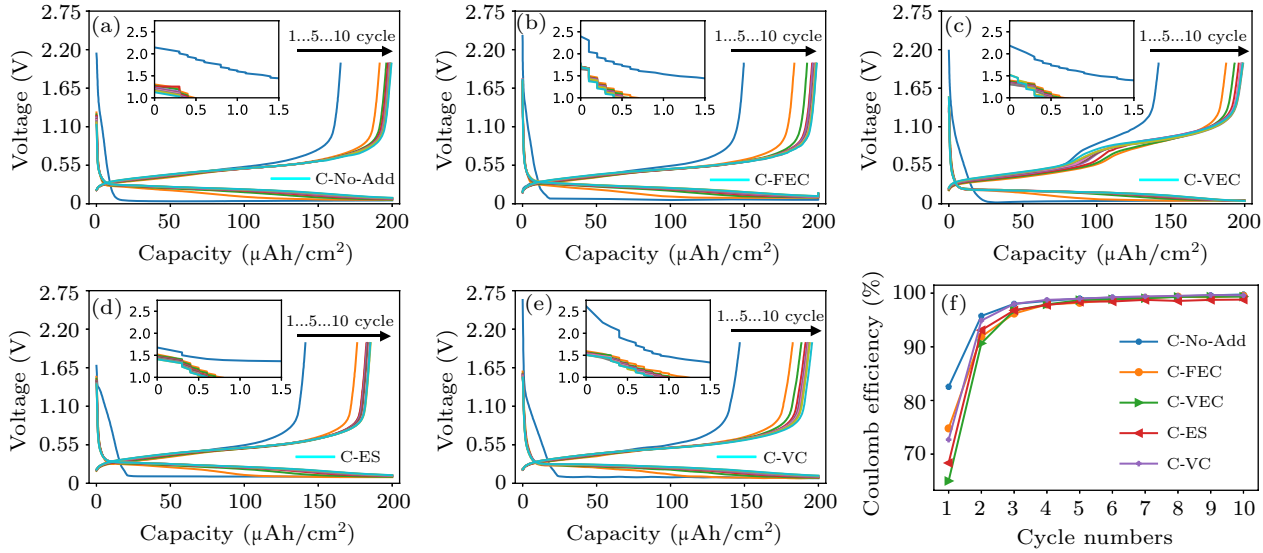


Fig. 3. Charge and discharge curve in 10 cycles with (a) No-Add, (b) FEC, (c) VEC, (d) ES, and (e) VC. The inset shows the portion of initial charge voltage with all cells. (f) Coulombic efficiency of half-cells with different electrolyte additives.

The higher the Coulombic efficiency is, the higher the initial charge voltage is, and the initial charge voltage contradicts the inconsistent Coulombic efficiency. 1) The Coulombic efficiency of the cells with the additive was not improved compared to the cells without the additive. 2) The initial charge voltage of the cell with the additive was higher than the initial charge voltage of the cell without the additive. 3) The addition of additives reduced the decrease in the initial charge voltage of the battery, which is in line with expectations. Further EIS and SEM characterization is required to analyze the role of additives at the working electrode surface in the cell.

To better understand the SEI film performance of these electrode surfaces, EIS measurements were performed on the fully charged electrodes. All measurements were taken after full delithiation, when the open-circuit potentials of the electrodes reached 2 V. The Nyquist plots of the C-No-Add, C-FEC, C-VEC, C-ES, and C-VC at the tenth cycle are shown in Fig. 4. The high-frequency semicircle relates to the resistance to Li^+ migration through the SEI layer (R_{sei}), the medium-frequency semicircle relates to the charge transfer resistance between the SEI layer and electrode interface (R_{ct}), and the low-frequency semicircle is attributed to the Warburg impedance (diffusion of Li^+ in the electrode) and insertion capacitance (accumulation of Li^+ in the electrode).[34] The impedance curves of C-No-Add in Fig. 4 show that the slope of the sloping line in the low-frequency region is less than 45°, indicating that the solid-state diffusion rate of lithium ions into the Si pillar becomes lower, resulting in an increase in the polarization of the electrode and causing a decrease in the initial charge voltage of C-No-Add.[35] The slope of the sloping line in the low-frequency region of the EIS curves of C-FEC, C-VEC, C-ES, and C-VC is higher than 45°. The introduction of the additive in Fig. 3 slowed down the initial trend of charge voltage decrease. The angle of the low-frequency curve should be maintained at 45° in EIS curve of ideal electrode. The main reason for the angle deviation from 45° of the low-frequency curve is the roughness of the electrode surface, and the diffusion process is partly equivalent to the spherical diffusion. Since the angle of the low-frequency region of the EIS curve of electrolyte additives is closer to 45° than that without electrolyte additives, the introduction of electrolyte additives can reduce the roughness of the electrode surface and show lower lithium-ion diffusion impedance under the same electrode material. According to the Thevenin model of lithium-ion battery, it can be concluded that the relationship between the initial discharge voltage and the open circuit voltage of the battery is affected by the ohmic resistance and the polarization resistance. The decrease of the polarization resistance will alleviate the decrease of the initial discharge voltage of the lithium-ion battery.

Since the main role of the additives is to form SEI films on the surface of the Si pillars, more attention was given in this study to the R_{sei} impedances displayed in the EIS of C-No-Add, C-FEC, C-VEC, C-ES, and C-VC, as shown in Table S1. The R_{sei} film impedances of C-FEC, C-VEC, C-ES, and C-VC are lower than that of C-No-Add. The R_{sei} film impedance of C-FEC, C-VEC, C-ES, and C-VC is one order of magnitude lower than that of C-No-Add. Based on the Thevenin equivalent circuit model of lithium-ion battery,[36] the ohmic resistance and polarization resistance affect the initial charge voltage and open circuit voltage, and the influence of the roughness of the electrode morphology and the consumption of the electrolyte on the ohmic resistance and polarization resistance changes the initial charge voltage of the lithium-ion battery (the parameter of the fitting curve is show in Table S3).

Through the collection of the initial charge voltage for 10

cycles, it is found that the faster the drop of the initial charge voltage, the faster the increase in the internal impedance of the electrode, which also indirectly reflects the increase in the rate of change of the working electrode and electrolyte loss. Since the loss of the electrode is caused by the generation of irreversible side reactions and the powdering failure of the working electrode, the capacity and Coulombic efficiency of the battery decrease. In the EIS impedance spectrum, a larger internal impedance of the electrode can be observed. Also, C-No-Add shows a larger R_{sei} impedance, and its initial charge voltage is lower than that of the other four batteries containing additives, but it presents a higher Coulombic efficiency, which is an abnormal phenomenon. It is necessary to observe the morphology of the Si pillar surfaces of C-No-Add, C-FEC, C-VEC, C-ES, and C-VC.

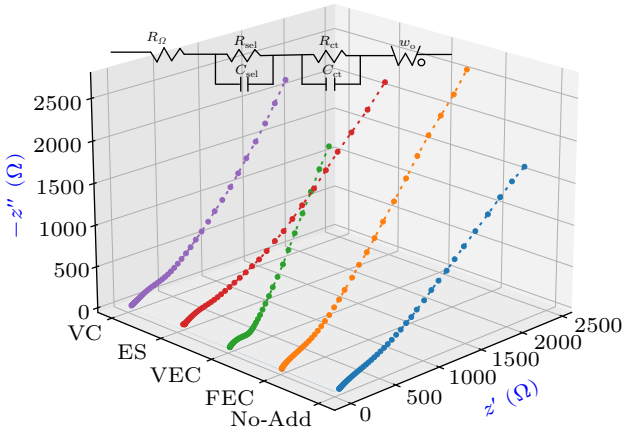


Fig. 4. Nyquist plots of silicon micropillar array electrodes after 10 charge/discharge cycles in five electrolytes.

The crystal orientation of the Si electrode used in this article is ⟨100⟩ in four mutually perpendicular ⟨110⟩ directions (red line) and four ⟨100⟩ directions (purple line) at an angle of 45°, as shown in Fig. 5(f). The interplanar spacing of crystalline Si along the ⟨110⟩ direction is greater than the interplanar spacing along the ⟨100⟩, ⟨111⟩, and ⟨211⟩ directions, providing the main lithium-ion diffusion channel, which is more significant in the ⟨110⟩ direction expansion.[37] Figures 5(a)–5(e) show the SEM images of C-No-Add, C-FEC, C-VEC, C-ES, and C-VC at 10 cycles. The surface of the C-No-Add Si electrode showed cross-shaped cracking and pulverization, and the surface of the Si pillar was much rougher. The Si pillars of C-FEC, C-VEC, C-ES, and C-VC were intact, and no cracking or pulverization was observed. The electrode surfaces of C-FEC, C-VEC, and C-ES were rough. C-VC showed cross-shaped expansion with smooth surfaces. In addition, the C-No-Add substrate exhibited a large crack with multilayer cracking, mainly due to the poor toughness of the SEI film (Fig. S3). The substrates of the electrodes were also observed, and it was found that only the substrate of C-No-Add was severely cracked. The surfaces of the remaining four electrolyte additive Si substrates were intact and consistent with the surfaces of the Si pillars of the corresponding additives (the volume expansion rate is shown in Table S2). Since the electrode substrate was a Si substrate and the counter electrode was a lithium sheet, the materials provided sufficient active Si and Li^+ to resist the decrease in Coulombic efficiency due to the side reaction of the Si electrode with the electrolyte. This is an important reason why C-No-Add shows better Coulombic efficiency and higher impedance in the tested Coulombic efficiency. However, the substrate cannot overcome the volume change due to the dead lithium capacity caused by the low diffusion coefficient of the electrode, while the Si micropillar electrode is better at overcoming this drawback. The accumulation of dead lithium during cell cycling can be attributed to the cracking and pulverization of the Si pillar of C-No-Add observed in Fig. 5(a). The accumulation of dead lithium decreases the rate of lithiation/delithiation and

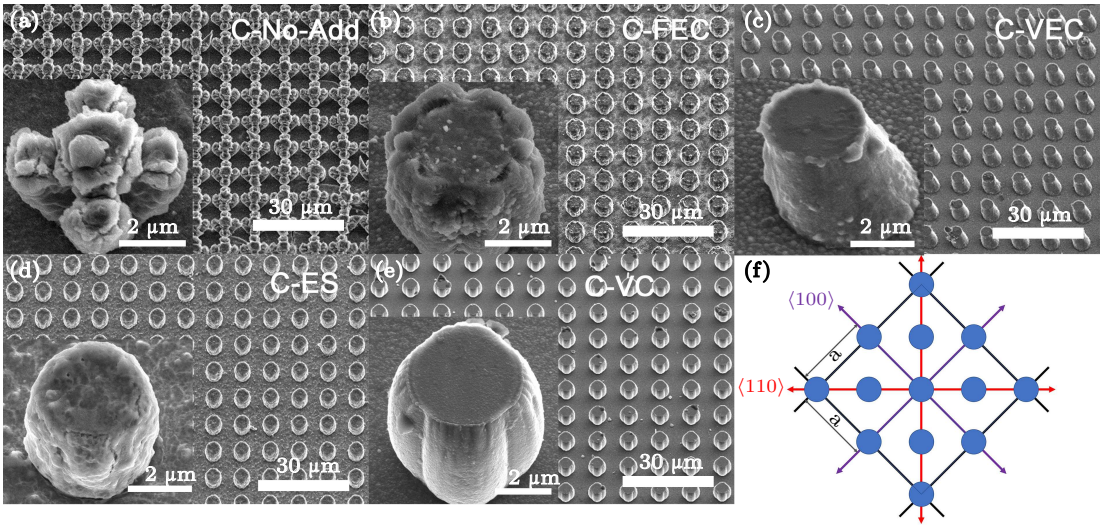


Fig. 5. (a)–(e) SEM images of Si micropillar array electrodes after 10 charge/discharge cycles in five electrolytes. (f) Schematic diagram of the atomic distribution of crystal Si ⟨100⟩ crystal plane.

increases the lithium-ion concentration polarization, which leads to a higher diffusion impedance (w_o) inside the Si pillar. However, lack of additives results in the formation of a thicker SEI film,[38] leading to higher R_{sei} film impedance on the electrode surface. Therefore, the electrode exhibits higher polarization impedance and lower initial charge voltage in the EIS test and charge/discharge cycle curves. The enhanced cyclability of the cell with additives compared to that of C-No-Add could be ascribed to the high toughness of the SEI film, which helps to maintain the complete morphology of the Si micropillar electrode against the large volume variation experienced during the prolonged charge/discharge processes.[39] Therefore, the use of additives can effectively protect Si pillars from cracking and pulverization. It is also shown that the electrochemical performance is closely related to the components of the electrolyte additives.[40]

To probe the lithiation/delithiation electrochemistry of the cells with different electrolyte solutions, cyclic voltammetry was measured at potential scan rates from 0.05 to 0.2 mV/s between 2 and 0.01 V versus Li^+/Li in a coin cell assembly after 10 cycles, as seen in Figs. 6(a)–6(e). As shown in Figs. 6(a)–6(e), a cathodic peak appeared at 0.10 V, which corresponds to $Li_{15}Si_4$ formations.[41] Two anodic peaks were clearly observed at approximately 0.38 V and 0.55 V, which correspond to the Li_xSi_y phase and then fully delithiated Si, respectively.[42] The peak position of the delithiation in the CV curve is the same as that of the dQ/dV (Fig. S1) peak position obtained by differentiation of the discharging curve. As the potential scan rate increases, the electrochemical reaction polarization increases and changes from reversible to quasi-reversible, reflecting that the internal conductivity of the electrode material limits the kinetic properties of lithium ions in Si-based materials.

Based on the relationship of the cyclic volumetric scan rate ($v^{1/2}$) versus the peak current (I_p), the lithium-ion diffusion coefficient of No-Add, FEC, VEC, ES, and VC can be calculated by the Randles–Sevcik equation[43]

$$I_p = 2.69 \times 10^5 \times n^{\frac{3}{2}} \times A \times D_0^{\frac{1}{2}} \times \upsilon^{\frac{1}{2}} \times C_0, \quad (1)$$

where n refers to the number of electrons per species in the reaction (1 for Li^+), A refers to the surface area of the electrode, D is the diffusion coefficient of Li^+ in the electrode, and C is the bulk concentration of Li^+. The fitting results of No-Add, FEC, VEC, ES, and VC are presented in Fig. 6(f). For No-Add, FEC, VEC, ES, and VC electrolytes, a linear relationship between peak currents (I_p) and the square root of the scan rate ($v^{1/2}$) shows that the lithiation/delithiation processes are diffusion-limited for the lithium ions. Based on Randles–Sevcik equation and utilizing the fitting curve to compare the diffusion relationship for five cells, we obtained $D_{No\text{-}Add} : D_{FEC} : D_{VEC} : D_{ES} : D_{VC} = 30 : 133 : 64 : 93 : 135$. It can be seen from Fig. 6(f) that C-No-Add has the lowest ion diffusion coefficient, indicating that the kinetic performance of Li^+ intercalation/detachment is the lowest; this low kinetic performance is caused by the polarization initiated by the SEI film. This observation is consistent with the cracking and pulverization of the C-No-Add Si column observed by SEM, which leads to a decrease in the initial charge voltage of the battery and the highest R_{sei} film impedance on the electrode surface in the EIS test. The diffusion coefficient of the sample with the additive is higher than that without the additive, which indicates that the polarization of the SEI film on the surface of the Si column is smaller, which is consistent with the integrity of the surface structure of the Si column observed for the electrode with additives in Figs. 5(b)–5(e).

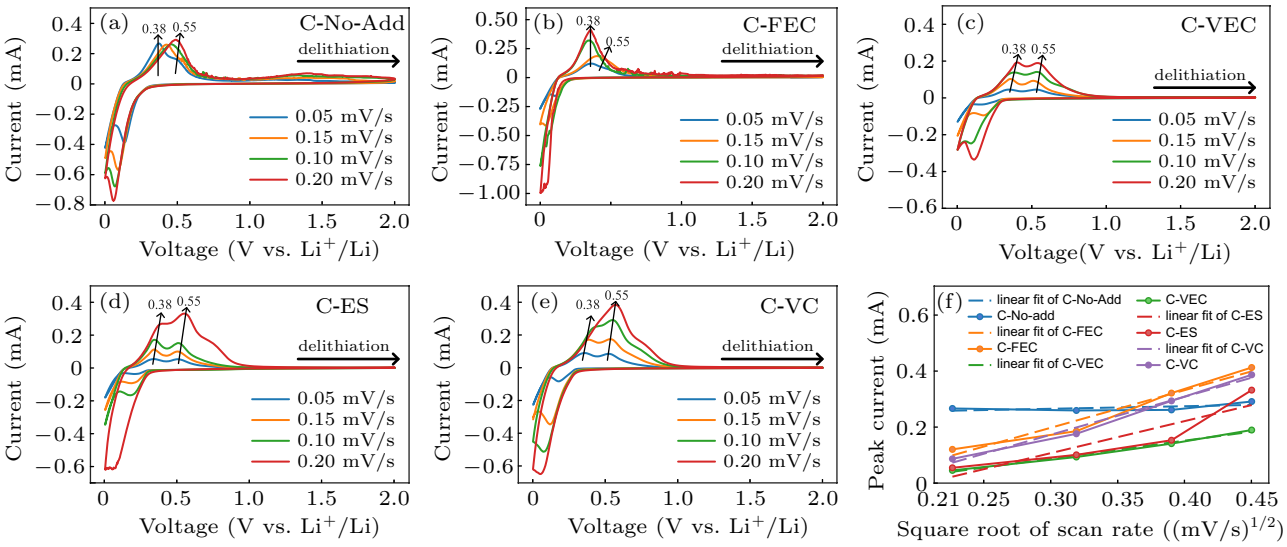


Fig. 6. (a)–(e) Cyclic voltammetry curves of different additives at different scanning rates after the tenth cycle. (f) The relationship of peak current and the square root of potential ($v^{1/2}$) scan rate for anodic peaks.

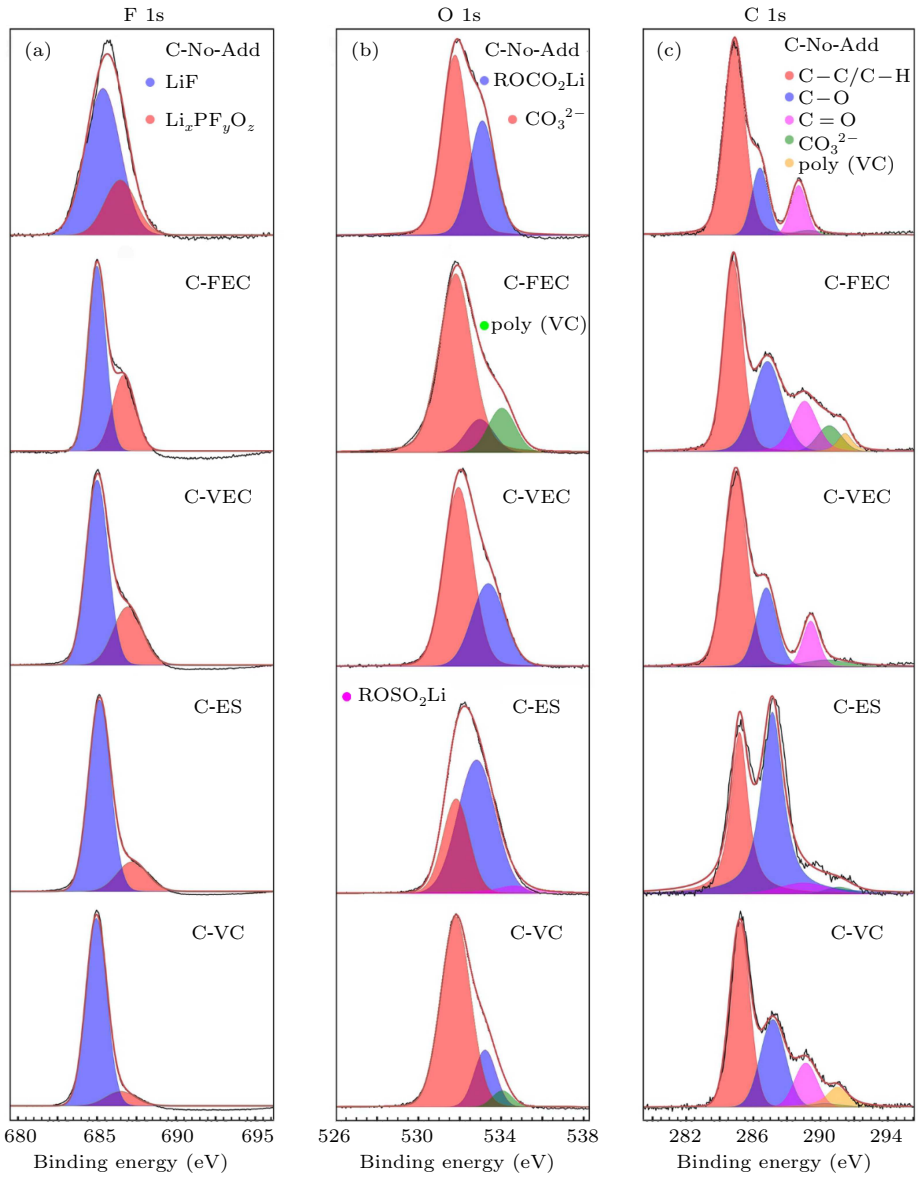


Fig. 7. (a) F 1s, (b) O 1s, and (c) C 1s high-resolution XPS spectra of surface films formed on Si micropillar array electrodes after 10 cycles in five electrolyte solutions.

Because the composition of surface films plays a significant role in determining the morphology of Si micropillars after cycling, it is necessary to understand the surface chemistry of the Si micropillar array electrodes in the electrolyte solutions studied herein. For this purpose, the cycled electrodes were characterized using *ex situ* XPS. The high-resolution XPS spectra measured from the Si micropillar array and cycled in five electrolyte solutions (Fig. 7) exhibit a significant analog in the composition of the surface films. The F 1s XPS core spectra (Fig. 7(a)) reveal the existence of two distinct peaks at 685 eV and 687 eV associated with LiF and $Li_xPF_yO_z$, respectively.[44] Two peaks of 531.8 eV and 533 eV can be seen in the detailed O 1s spectrum, which correspond to the oxygen in the carbonate compound and oxygen in $ROCO_2Li$, respectively.[45] For the pristine composite electrode (Fig. 7(b)), the C 1s peaks at 285 eV, 286.9 eV, 288.6 eV, and 290 eV correspond to C–C/C–H (hydrocarbons), C–O (Li ethers), C=O (alkoxy carbons), and CO_3^{2-} (Li_2CO_3/$ROCO_2Li$), respectively.[46,47] The obvious difference between the spectra is the existence of an extra peak for the C-FEC and C-VC at 290.8 eV corresponding to the carbonate C atom of poly-(VC).[48,49] It is shown in the Li 1s spectrum that the surface films formed by all electrolytes contain LiF at 56 eV and a small amount of Li_2CO_3 at 55.6 eV (as shown in Fig. S4). The peak position at 54 eV is resolved in the Li 1s spectrum, and only the C-VC surface contains Li_2O.[50]

All the electrode surface SEI film compositions contained both inorganic and organic lithium salts but not in the same proportion. While dense inorganic lithium salt-dominated SEI films were formed in the first cycle, fluffy organolithium salt-dominated SEI films or dense inorganic lithium salt-dominated SEI films were formed in subsequent cycles.[40] The surface compositions of C-No-Add and C-VEC were similar, but the

inorganic lithium salt content on the surface of C-No-Add was significantly lower than that of C-VEC. Less inorganic lithium salt provided a less dense SEI film, resulting in electrolyte infiltration that caused the electrode to continuously consume active Si on the surface of the Si column, and the products formed by this side reaction increased the thickness of the electrode surface, resulting in a decrease in the diffusion kinetics of lithium ions. This was directly manifested by the increase in dead lithium capacity in the Si pillar after multiple cycles of the electrode, which led to the expansion and fragmentation of the Si column, resulting in a higher polarization impedance of the cell. The interception of Li expands the volume of the silicon electrode, resulting in the rupture and repeated formation of the SEI film formed on the surface of the electrode. The thickness of the SEI films on the surface of the electrode increases, which further increases the lithiation/delithiation distance from Li^+ in the silicon electrode, thereby increasing the electrode concentration polarization. The use of VEC increased the inorganic lithium salt concentration on the electrode surface, which made the SEI film on the electrode surface denser and greatly reduced the occurrence of side reactions between the electrode and the electrolyte, resulting in a lower impedance and a more complete Si column surface compared to that of C-No-Add. The surface compositions of the C-FEC and C-VC electrodes were similar, but the C-VC surface exhibited a lower organolithium salt composition, consistent with the fluffier surface of C-FEC and smoother surface of C-VC observed in the SEM images. Meanwhile, the silica columns were not chalked, which was due to the improved mechanical properties of the SEI film by the formation of poly-(VC) on the surface (as shown in Scheme S1).[50] More organolithium salts on the surface were observed in C-ES, but the Si pillar did not crack like that in C-No-Add. This outcome may be because sulfide formed on the surface increases the mechanical properties and stability of the SEI film so that the electrode polarization is lower with increasing cycle periods.[51]

4. Conclusion and perspectives

In conclusion, the Si micropillar platform was used to test the electrolyte solutions of four additives (FEC, VEC, ES, and VC) in half-cells by charge/discharge tests, CV, SEM characterization, and XPS surface analysis. The enhanced electrochemical performance of the Si micropillar arrays in electrolyte solutions containing additives was attributed to the superior performance of the surface films formed during electrochemical cycling. A comprehensive analysis of the results from XPS, SEM, and electrochemical tests showed that the additives were mainly optimized for the SEI film composition. The inorganic lithium salts formed a smoother and flatter film, while a higher organic lithium salt content resulted in a rougher electrode surface, as shown by the Si pillar morphology. The polylithium salt component in the SEI film can further reduce the R_{sei} impedance of the SEI film and enhance the diffusion coefficient of lithium ions. Such a Si micropillar platform and analytical methods enable the in-depth analysis of the comprehensive performance of additives, thereby providing a guiding principle for developing high performance additives for LIBs with a high-energy density.

References

[1] Armand M and Tarascon J M 2008 *Nature* **451** 652
[2] Han B, Yang Y, Shi X B, Zhang G Z, Gong L, Xu D W, Zeng H B, Wang C Y, Gu M and Deng Y H 2018 *Nano Energy* **50** 359
[3] Yuan C Z, Wu H B, Xie Y and Lou X W 2014 *Angew. Chem.-Int. Ed.* **53** 1488
[4] Qin X Y, Yan B Y, Yu J, Jin J, Tao Y, Mu C, Wang S C, Xue H G and Pang H 2017 *Inorg. Chem. Front.* **4** 1424
[5] Zuo X X, Wang X Y, Xia Y G, Yin S S, Ji Q, Yang Z H, Wang M M, Zheng X F, Qiu B, Liu Z P, Zhu J, Muller-Buschbaum P and Cheng Y J 2019 *J. Power Sources.* **412** 93
[6] Bates J B, Dudney N J, Neudecker B, Ueda A and Evans C D 2000 *Solid State Ion.* **135** 33
[7] Mills E, Cannarella J, Zhang Q, Bhadra S, Arnold C B and Chou S Y 2014 *J. Vac. Sci. Technol. B* **32** 06FG10
[8] Choi J H, Kim H K, Jin E M, Seo M W, Cho J S, Kumar R V and Jeong S M 2020 *J. Hazard. Mater.* **399** 122949
[9] Wang J, Wang X, Liu B, Lu H, Chu G, Liu J, Guo Y G, Yu X, Luo F, Ren Y, Chen L and Li H 2020 *Nano Energy* **78** 105101
[10] Im J, Jang E K, Kim S, Yoon S, Kim D H and Cho K Y 2020 *Chem. Eng. J.* **402** 126292
[11] Feng X, Yang J, Bie Y, Wang J, Nuli Y and Lu W 2014 *Nanoscale* **6** 12532
[12] Kim I S and Kumta P N 2004 *J. Power Sources.* **136** 145
[13] Majeed M K, Saleem A, Ma X J and Ma W Z 2020 *J. Alloys Compd.* **848** 156590
[14] Fan Z Q, Zheng S S, He S, Ye Y Y, Liang J H, Shi A D, Wang Z L and Zheng Z F 2020 *Diamond Relat. Mater.* **107** 107898
[15] Wang C, Luo F, Lu H, Liu B A, Chu G, Quan B G, Li J J, Gu C Z, Li H and Chen L Q 2017 *Nanoscale* **9** 17241
[16] Schnabel M, Harvey S P, Arca E, Stetson C, Teeter G, Ban C M and Stradins P 2020 *ACS Appl. Mater. Interfaces* **12** 27017
[17] Keles O, Karahan B D, Eryilmaz L, Amine R, Abouimrane A, Chen Z H, Zuo X B, Zhu Z H, Al-Hallaj S and Amine K 2020 *Nano Energy* **76** 105094
[18] Hasa I, Haregewoin A M, Zhang L, Tsai W Y, Guo J H, Veith G M, Ross P N and Kostecki R 2020 *ACS Appl. Mater. Interfaces* **12** 40879
[19] Zou F and Manthiram A 2020 *Adv. Energy Mater.* **10** 2002508
[20] Zhang Q Y, Zhang C F, Luo W W, Cui L F, Wang Y J, Jian T Y, Li X L, Yan Q Z, Liu H D, Ouyang C Y, Chen Y L, Chen C L and Zhang J J 2020 *Adv. Sci.* **7** 2000749
[21] Li Z H, Zhang Y P, Liu T F, Gao X H, Li S Y, Ling M, Liang C D, Zheng J C and Lin Z 2020 *Adv. Energy Mater.* **10** 1903110
[22] Michan A L, Parimalam B S, Leskes M, Kerber R N, Yoon T, Grey C P and Lucht B L 2016 *Chem. Mater.* **28** 8149
[23] Haruta M, Hioki R, Moriyasu T, Tomita A, Takenaka T, Doi T and Inaba M 2018 *Electrochim. Acta* **267** 94
[24] Chen L, Wang K, Xie X and Xie J 2007 *J. Power Sources.* **174** 538
[25] Zheng X, Fang G, Pan Y, Li Q and Wu M 2019 *J. Power Sources.* **439** 227081
[26] Jin Y, Kneusels N H, Marbella L E, Castillo-Martinez E, Magusin P, Weatherup R S, Jonsson E, Liu T, Paul S and Grey C P 2018 *J. Am. Chem. Soc.* **140** 9854
[27] Schwenke K U, Solchenbach S, Demeaux J, Lucht B L and Gasteiger H A 2019 *J. Electrochem. Soc.* **166** A2035
[28] Madec L, Petibon R, Tasaki K, Xia J, Sun J P, Hill I G and Dahn J R 2015 *Phys. Chem. Chem. Phys.* **17** 27062
[29] Xia J, Aiken C P, Ma L, Kim G Y, Burns J C, Chen L P and Dahn J R 2014 *J. Electrochem. Soc.* **161** A1149
[30] Xiang H, Chen J and Wang H 2011 *Ionics* **17** 415

[31] Pan Y C, Saikia D, Fang J, Tsai L D, Fey G T K and Kao H M 2014 *Rsc. Advances* **4** 13293
[32] Yi R, Dai F, Gordin M L, Sohn H and Wang D H 2013 *Adv. Energy Mater.* **3** 1507
[33] Xu K 2014 *Chem. Rev.* **114** 11503
[34] Tao H C, Zhu S C, Xiong L Y, Zhang L L and Yang X L 2017 *Chemistryselect* **2** 2832
[35] Ratynski M, Hamankiewiecz B, Krajewski M, Boczar M, Buchberger D A and Czerwinski A 2019 *Electrocatalysis* **11** 160
[36] He H W, Xiong R, Zhang X W, Sun F C and Fan J X 2011 *IEEE Trans. Veh. Technol.* **60** 1461
[37] Liu X H, Wang J W, Huang S, Fan F F, Huang X, Liu Y, Krylyuk S, Yoo J, Dayeh S A, Davydov A V, Mao S X, Picraux S T, Zhang S L, Li J, Zhu T and Huang J Y 2012 *Nat. Nanotechnol.* **7** 749
[38] Luo F, Chu G, Xia X X, Liu B N, Zheng J Y, Li J J, Li H, Gu C Z and Chen L Q 2015 *Nanoscale* **7** 7651
[39] Zhang Q and White R E 2008 *J. Power Sources.* **179** 793
[40] Huang W, Attia P M, Wang H S, Renfrew S E, Jin N, Das S, Zhang Z W, Boyle D T, Li Y Z, Bazant M Z, McCloskey B D, Chueh W C and Cui Y 2019 *Nano Lett.* **19** 5140
[41] Li H, Huang X J, Chen L Q, Zhou G W, Zhang Z, Yu D P, Mo Y J and Pei N 2000 *Solid State Ion.* **135** 181
[42] Bruce P G, Scrosati B and Tarascon J M 2008 *Angew. Chem.-Int. Ed.* **47** 2930
[43] Ai Q, Li D P, Guo J G, Hou G M, Sun Q, Sun Q D, Xu X Y, Zhai W, Zhang L, Feng J K, Si P C, Lou J and Ci L J 2019 *Adv. Mater. Interfaces* **6** 1901187
[44] Nguyen C C and Lucht B L 2014 *J. Electrochem. Soc.* **161** A1933
[45] Aurbach D, Gamolsky K, Markovsky B, Gofer Y, Schmidt M and Heider U 2002 *Electrochim. Acta* **47** 1423
[46] Aupperle F, Eshetu G G, Eberman K W, Xioa A, Bridel J S and Figgemeier E 2020 *J. Mater. Chem. A* **8** 19573
[47] Wu R, Liu X Q, Zheng Y J, Li Y H, Shi H F, Cheng X P, Pfleging W and Zhang Y F 2020 *J. Power Sources.* **473** 228481
[48] Kennedy T, Brandon M, Laffir F and Ryan K M 2017 *J. Power Sources.* **359** 601
[49] El Ouatani L, Dedryvere R, Siret C, Biensan P, Reynaud S, Iratcabal P and Gonbeau D 2009 *J. Electrochem. Soc.* **156** A103
[50] Etacheri V, Haik O, Goffer Y, Roberts G A, Stefan I C, Fasching R and Aurbach D 2012 *Langmuir* **28** 965
[51] Ota H, Sato T, Suzuki H and Usami T 2001 *J. Power Sources.* **97–98** 107